


Article

Deformation Coupled Effective Permeability Change in Hydrate-Bearing Sediment during Depressurization

Xiang Sun ^{1,2}, Hao Luo ^{3,*} and Kenichi Soga ^{2,*}¹ Institute of Rock and Soil Mechanics, Chinese Academy of Sciences, Wuhan 430071, China² Department of Civil and Environmental Engineering, University of California, Berkeley, CA 94701, USA³ China Construction Science & Technology Group Co., Ltd., Shenzhen Branch, Shenzhen 518054, China* Correspondence: luo.h@cscec.com (H.L.); soga@berkeley.edu (K.S.)

Abstract: Methane hydrates found in the sediments of deep sea and permafrost regions draw global interest. The rate of gas production from a depressurized well is governed by the effective permeability of the hydrate-bearing sediments around the wellbore. During depressurization, a decrease in pore pressure leading to soil compaction and hydrate dissociation results in a dynamic change in the effective permeability. To describe the change in the effective permeability in detail, in this study, a simple coupled compressibility–permeability analysis method is proposed to identify the conditions under which the effective permeability increases or decreases after depressurization. An analytical solution is derived for the effective permeability change with pore pressure and temperature, considering hydrate dissociation and soil compaction. We found that when there is a sufficient heat supply, hydrate dissociation dominates the effective permeability during hydrate dissociation, but after hydrate dissociation, soil compaction is the governing factor for permeability change. When there is an insufficient heat supply, however, compaction mainly determines the permeability, and the effect of hydrate dissociation is limited. This work will be helpful for rapid reservoir assessment.



Citation: Sun, X.; Luo, H.; Soga, K. Deformation Coupled Effective Permeability Change in Hydrate-Bearing Sediment during Depressurization. *Processes* **2022**, *10*, 2210. <https://doi.org/10.3390/pr10112210>

Academic Editor: Chengtung Chou

Received: 11 September 2022

Accepted: 16 October 2022

Published: 27 October 2022

Publisher's Note: MDPI stays neutral with regard to jurisdictional claims in published maps and institutional affiliations.



Copyright: © 2022 by the authors. Licensee MDPI, Basel, Switzerland. This article is an open access article distributed under the terms and conditions of the Creative Commons Attribution (CC BY) license (<https://creativecommons.org/licenses/by/4.0/>).

Keywords: effective permeability; hydrate dissociation; depressurization; soil compaction; heat supply

1. Introduction

Methane hydrates found in the sediments of deep sea and permafrost regions draw global interest as an alternative energy resource to traditional fossil-based energy. It is conservatively estimated that the amount of organic carbon stored in methane hydrate reservoirs is about twice that of all other fossil fuels on the planet, including coal, oil and natural gas [1]. Unlike oil and natural gas stored in rock formations, methane hydrates buried beneath the deep sea are present in relatively loose sediments and play an important role in the strength of marine sediment structure [2–5]. Hydrate production may damage the sediment structure and it poses a challenge to production safety [6,7]. Therefore, in recent years, only a few field-production trials were conducted to assess the feasibility of extracting methane gas from hydrates that are buried under deep water sediments [8,9].

The majority of current trials in deep water use the depressurization method, which reduces the pore fluid pressure from a production wellbore and dissociates hydrate to methane gas and water. The gas released in-situ then migrates toward the wellbore by pressure gradient and is extracted from the production well. To achieve a high rate of gas production by depressurization, the permeability of hydrate-bearing sediments (HBSs) must be large enough to bring the released gas to the production well. It is also important to note that hydrate dissociation is an endothermic process, requiring heat from the surrounding environment. Therefore, during depressurization operation, heat flows to hydrate locations by both conduction and convection, and a high rate of dissociation

requires the latter component to be a dominant factor [10]. Low permeability slows the propagation of reduced pressure and heat transport, leading to difficulty in hydrate dissociation and low energy-production efficiency [11].

The permeability of HBSs was investigated both experimentally and numerically. Masuda [12] proposed the University of Tokyo model, in which the ratio of the permeability of HBSs to that of the host sediment without hydrate is a power expression of $1 - s_h$,

$$K = (1 - s_h)^N \quad (1)$$

where K is the relative permeability for hydrate, s_h is the hydrate saturation and N is the power. Minagawa et al. [13] measured the water permeability of HBSs with different hydrate saturations and proposed a model to describe the relationship between hydrate saturation and permeability. Nimblett et al. [14] derived a formula for estimating permeability based on the Kozeny–Carman model to analyze the permeability evolution during hydrate formation. Kumar et al. [15] combined numerical simulations and experiments to evaluate the gas permeability of HBSs. They applied the Kozeny–Carman model to derive an expression, which is equivalent to the University of Tokyo model with the coefficient N being equal to 3. However, this expression is only applicable when hydrate saturation is less than 0.35. Delli et al. [16] introduced a hybrid modeling approach to use multiple models to better predict the permeability variation. In this model, two relative permeabilities obtained from Kozeny’s grain-coating and pore-filling models are proposed to describe the effects of different hydrate occurrence habits. Liang et al. [17] proposed a three-dimensional cubic pore network model to study the effect of hydrate particles and its growth habit on the permeability. Katagiri et al. [18] formulated Kozeny–Carman-based permeability reduction models for two types of particle pack and used computational fluid dynamics (CFD) simulation coupled with the discrete element method (DEM) to evaluate the influence of hydrate saturation and morphology on tortuosity. Kossel et al. [19] tested the five most well-known permeability equations, and found that all the suitable permeability equations included the term $(1 - s_h)^N$ and derived a high exponent N .

The physical validity of the above-mentioned permeability models for HBSs was well discussed in the past. Johnson et al. [20] thoroughly investigated the effective permeability of HBS specimens retrieved from the Mount Elbert test and found that moderate hydrate saturation (1.5–36%) reduced the permeability of the HBS. Kneafsey et al. [21] used X-ray computed tomography to observe location density changes due to hydrate formation and flowing water, and further investigated the increase in the effective permeability of HBS with increasing pore space size. They found that water flux was enhanced by increased capillary suction and pointed out that the hydrate does not, in general, behave like a residual gas in a water-saturated porous medium. Jiang et al. [22] innovatively carried out CT to extract a pore model and calculated the absolute permeability with a high level of accuracy. Liu et al. [23] conducted a series of laboratory-scale tests to investigate the influence of hydrate saturation and effective stresses on the gas phase permeability of kaolin clay and found a critical hydrate saturation for the gas phase permeability of hydrate-bearing clayey specimen. Daigle et al. [24] investigated relative permeability to water and gas in the presence of hydrates in sediments. They discovered a link between pore structure and the transport properties of HBSs. Li et al. [25] found a new relationship between the ratio of permeability in the presence and absence of hydrate and hydrate saturation, based on their experimental data for quartz sands.

In recent years, many researchers combined numerical and experimental methods to study multi-scale characteristics of HBSs. Xu et al. analyzed the influence of hydrate distribution on the permeability of HBSs at the pore scale [26]. Lei et al. proposed a new cubic model to calculate the permeability influenced by hydrate decomposition [27]. Liu et al. clarified the relationship between permeability and hydrate saturation using the lattice Boltzmann method (LBM) [28]. Hu et al. used CT scanning and pore network modeling (PNM) to analyze the influence mechanism of the permeability anisotropy of sandy sediment before and after hydrate generation [29,30]. In terms of laboratory exper-

iments, Wu et al. and Liu et al. discussed the influence law of the ratio of sand to soil and the stress sensitive effect on dynamic permeability, clarifying the characteristics of non-Darcy dynamic seepage in the aqueous phase in HBSs [31,32]. Based on a novel X-ray triaxial testing apparatus, Wu et al. and Zhou et al. clarified the microstructure evolution of HBSs during shear, creep and isotropic consolidation processes, and revealed dynamic permeability evolution in detail, which is crucial for improving the prediction accuracy of gas–water production from a hydrate reservoir [31,33–35]. An innovative method was proposed for permeability determination with hydrate phase transition by using NMR: the results showed accurate predictions of relative permeability related to variations in pore structure and hydrate saturation [36].

When the depressurization method is adopted, the rate of gas production from a depressurized well is governed not only by the magnitude of pressure drawdown, but also by the permeability around the wellbore. Permeability changes both spatially and temporarily during depressurization and depends on both hydrate saturation and porosity change through soil compaction. The mechanism of the latter is that a decrease in pore pressure by depressurization leads to an increase in effective stress. This, coupled with the collapse of the hydrate-bonded soil structure by dissociation, results in volume compression, which in turn reduces permeability. However, this effect was often ignored in past studies. For example, Rutqvist et al. [37] introduced a porosity-dependent formula into the TOUGH + HYDRATE model but, in their simulation, the pore volume was fixed because they did not consider the effect of geomechanical behavior of HBSs on the change of porous volume. Based on the results of a series of simulations and experiments, Sakamoto et al. [38] proposed a new formula related to the effective permeability of HBSs, in which the contribution of change in the volume of sediment skeleton to the intrinsic permeability was considered. The effect of the reduction in permeability due to consolidation on the dissociation and gas production behavior was not obvious; this is because the scale of the simulated HBS was small and the effective permeability was relatively high. Chen et al. [39] systematically investigated the promoting effect of the permeability of HBSs during hydrate dissociation and proposed a novel enhancement strategy of water flow erosion for natural gas hydrate production.

Gupta et al. [40] proposed a formula for estimating effective permeability based on Rockhold's model [41] and Faruk's model [42] in order to test the performance of their thermo-hydro-mechanical model. However, they did not analyze the effect of compaction on the permeability of HBSs. Myshakin et al. [43] and Moridis et al. [44] found that higher pore compressibility decreases production rates because the permeability decreases with soil compaction. To simulate the compression-influenced gas production, they applied a pore compressibility defined in petroleum engineering to govern the change in porosity, further affecting the permeability and production rate. To investigate the relationship between compressibility and permeability, Yoneda et al. [45] conducted a series of consolidation tests. The results showed that the permeability dropped by 90% when the effective stress increased by 10 MPa due to the consolidation and clogging of fine particles which formed by particle breakage [46]. Therefore, the permeability drop due to soil consolidation cannot be neglected.

This study focuses on the changes in the effective permeability of HBSs during depressurization. The study considers two counteracting effects; (i) the permeability-reducing trend by soil compaction induced by the increase in effective stress and (ii) the permeability-increasing trend by the increase in fluid permeability due to hydrate dissociation inside the pores. This is achieved by combining (a) a power law model of void ratio–permeability relationship and (b) the University of Tokyo model of hydrate-saturation-dependent permeability. To illustrate the coupling effect, an analytical solution that relates permeability change to hydrate dissociation and soil compaction is derived, and a parametric study is conducted using this solution in two extreme scenarios (the constant temperature case and the heat-insulated case).

2. Modeling Method

2.1. A Relationship between Permeability and Void Ratio

Kozeny [47] proposed a model for describing the relationship between hydraulic conductivity and void ratio. Carman [48] and Matyka et al. [49] also proposed a similar form, which can be presented as follows

$$K_{\text{sat}} = C \frac{g}{\mu_w \rho_w} \frac{e^3}{S_s^2 G_s^2 (1 - e)} \quad (2)$$

where C is a constant related to the porous space geometry, g is acceleration of gravity, μ_w is the dynamic viscosity of water (Pa·s) related to temperature, ρ_w is the density of water, G_s is the specific gravity of the grained soil, S_s is the specific surface of the grained soil, and e is the void ratio.

The limitation of the above model for evaluating the permeability of sandy soils with fines and fine-grained soils was long recognized. For example, Terzaghi [50] pointed out that the limitation is owing to the thin immobile water layer at the surface of clay particles and the inaccurate estimation of the specific area of the fine particles and the pore size. To better fit the experimental data, Ren et al. [51] extended the relation in log–log scale and obtained the following relationship between the void ratio and hydraulic conductivity of saturated soils.

$$k_{\text{sat}} = k_{s0} \left(\frac{e}{e_0} \right)^\beta \quad (3)$$

where k_{sat} is the hydraulic conductivity for water-saturated soil, k_{s0} is the hydraulic conductivity corresponding to the initial void ratio e_0 and e is the void ratio. β is the curve fitting parameter. Ren et al. [51] rearranged the published data for natural and remolded sediments from coarse sands to fine-grained clays. They also investigated the relationship between the hydraulic conductivity and void ratio of different types of soils. By fitting the hydraulic conductivity data using Equation (3), they found that k_{s0} decreases for the finer sediment and the slopes κ for most soils are similar. Most of the β values are in the range of $2 < \beta < 6$; $\beta = 3 \pm 1$ for coarse-grained soils, whereas $\beta = 5 \pm 1$ for fine-grained soils.

Considering the relationship between permeability K and hydraulic conductivity k , in which $K = \frac{k \mu_w}{\rho_w g}$ where μ_w , ρ_w are viscosity and density of water, respectively, the following formula is given

$$K_{\text{int}} = K_{s0} \left(\frac{e}{e_0} \right)^\beta \quad (4)$$

where K_{s0} is the initial intrinsic permeability for the initial void ratio of e_0 and K_{int} is intrinsic permeability.

For HBSs, the occurrence of hydrate increases flow tortuosity. The concept of relative permeability is used to describe the decrease in permeability due to hydrate formation. Masuda et al. [12] introduced an exponent N to relate relative permeability K_{rh} to the hydrate saturation s_h :

$$K_{\text{rh}} = (1 - s_h)^N \quad (5)$$

The value of N is related to the occurrence habitat of the hydrate, pore size and the specific area of reaction [52].

Hence the expression of the effective permeability of HBSs is

$$K = K_{\text{int}} K_{\text{rh}} = K_{s0} \left(\frac{e}{e_0} \right)^\beta (1 - s_h)^N \quad (6)$$

The model has two state variables (void ratio and hydrate saturation) and three model parameters (β , N and K_{s0}). It shows that permeability decreases with decreasing void ratio but increases with decreasing hydrate saturation. In this paper, the relative effect of changes in e and s_h on the effective permeability K during a depressurization event is

considered. In this paper, we do not consider relative permeability for the different phases of fluid, so the effective permeability of HBSs is identical to the permeability of HBSs.

2.2. One-Dimensional Compression Model

During depressurization, the effective stress increases due to pore pressure reduction, and soil compaction occurs. The reduction in void ratio results in a permeability decrease. At the same time, the hydrate dissociates, resulting in a permeability increase. In this study, these counteracting changes in permeability during depressurization are examined. The study uses a simple 1D analytical model for the investigation. The 1D model will allow a quick estimation of settlement that may occur during depressurization. Figure 1a shows a 1D compression model of the HBS. Figure 1b shows that a pore pressure decrease leads to an increase in effective stress. It is assumed that the vertical overburden total stress σ_v remains constant. Hence, the vertical effective stress increment $\Delta\sigma'_v$ is opposite and equal to the pore pressure decrease ($\Delta p_p = -\Delta\sigma'_v$), according to the Terzaghi effective principle.

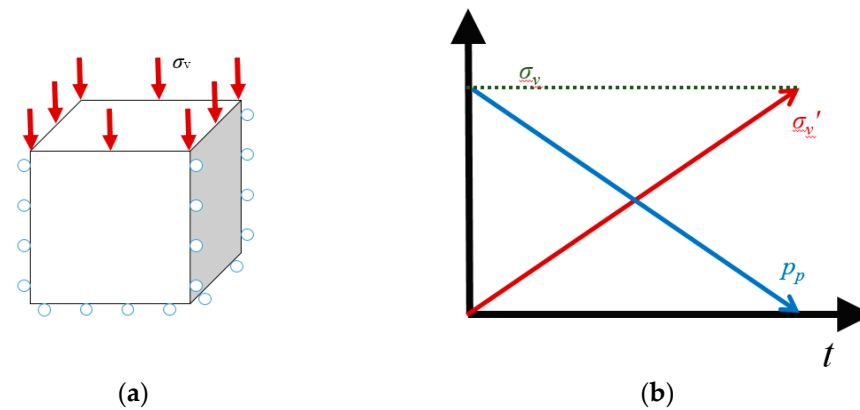


Figure 1. Compression model (a) 1D compaction model and (b) increase in effective stress with decreasing pore pressure.

The compression model of the sediment is shown in Figure 2, following the previous work of Uchida et al. [53]. The dashed line describes the compression behavior of a sediment that contains hydrate. The black solid line in Figure 2a is the normal compression line of the host sediment without hydrate and the dashed line describes the normal compression line of the HBS. The relative position of the two lines shows the enhancement of the yield stress of the sediment resulting from the hydrate bonded structure. The blue solid line is the recompression line, which is the nonlinear elastic compression behavior prior to yielding.

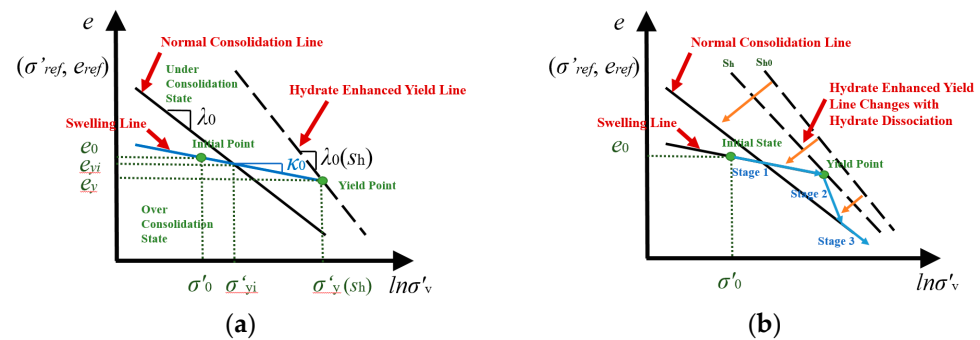


Figure 2. The sediment generally experiences three stages during depressurization and hydrate dissociation including (a) the hydrate effects on compression behavior and (b) stress state change during depressurization.

An HBS generally experiences the following three stages during depressurization, as shown in Figure 2b. In the first stage, the stress state is on a recompression line until it

reaches the yield point. In the second stage, yielding occurs and the stress state follows the normal compression line, which changes its position as the hydrate dissociates (shown by the orange arrows). In the final third stage, all the hydrate dissociates, and the stress state reaches the normal consolidation line of the host sediment. The stress state moves along the normal consolidation line of the host sediment without hydrate as the effective stress increases by depressurization.

Herein, the initial stress state of the sediment is (σ'_{v0}, e_0) , and it has a stress-history-dependent yield stress state of (σ'_{yi}, e_{yi}) when the sediment had no hydrate, as shown in Figure 2a. Along the recompression line, the following relationship holds

$$e_0 = e_{yi} - \kappa_0 \ln \left(\frac{\sigma'_{v0}}{\sigma'_{yi}} \right) \quad (7)$$

where κ_0 is the slope of the elastic recompression line. It is assumed that stiffness is not a function of hydrate saturation because the stiffness of a hydrate crystal is smaller than that of sediment grains.

The normal compression line of a sediment without hydrate is expressed using the following formula [54]

$$\sigma'_v = \sigma'_{yi} \exp \left(\frac{e_{yi} - e}{\lambda_0} \right) \quad (8)$$

where λ_0 is the slope of the normal consolidation line, which has an intercept of (σ'_{yi}, e_{yi}) at the yield point.

The existence of hydrate increases the density of the sediments and bonds the sediment particles, enhancing the sediment yield strength σ'_y . A relationship between σ'_y and hydrate saturation s_h was proposed [55]:

$$\sigma'_y = \sigma'_{yi} + as_h^b \quad (9)$$

where σ'_{yi} is the initial yield stress of the host sediment as defined earlier, and a and b are the coefficients governing the yield stress related to hydrate saturation s_h . The yield stress of an HBS is the sum of the stress-history-dependent yield stress and the increase in strength of the hydrate.

The expression of the hydrate-enhanced normal compression line becomes the following by combining Equations (8) and (9).

$$\sigma'_v = \sigma'_{yi} \exp \left(\frac{e_{yi} - e}{\lambda_0} \right) + as_h^b \quad (10)$$

This equation can be rewritten as

$$e = e_{yi} - \lambda_0 \ln \left(\sigma'_v - as_h^b \right) + \lambda_0 \ln \sigma'_{yi} \quad (11)$$

Substituting Equations (10) and (11) to eliminate e_{yi} , the following relationship between e and σ'_v is obtained.

$$e = e_0 + \kappa_0 \ln \sigma'_{v0} - \lambda_0 \ln \left(\sigma'_v - as_h^b \right) + (\lambda_0 - \kappa_0) \ln \sigma'_{yi} \quad (12)$$

Combining Equations (7) and (12), leads to the following.

$$K = K_{s0} \left(1 + \frac{\kappa_0 \ln \left(\frac{\sigma'_{v0}}{\sigma'_{yi}} \right) - \lambda_0 \ln \left(\frac{\sigma'_v - as_h^b}{\sigma'_{yi}} \right)}{e_0} \right)^\beta (1 - s_h)^N \quad (13)$$

Using Equation (4), the initial effective permeability is

$$K_0 = K_{s0}(1 - s_{h0})^N \quad (14)$$

Therefore,

$$\frac{K}{K_0} = \left(1 + \frac{\kappa_0 \ln\left(\frac{\sigma'_{v0}}{\sigma'_{yi}}\right) - \lambda_0 \ln\left(\frac{\sigma'_v - a s_h^b}{\sigma'_{yi}}\right)}{e_0} \right)^\beta \left(\frac{1 - s_h}{1 - s_{h0}} \right)^N \quad (15)$$

This equation shows how the effective permeability of HBS increases with hydrate dissociation (s_h decreases from s_{h0}) and decreases with an increase in vertical effective stress (σ'_v increases from σ'_{v0}) by depressurization. Normally, effective permeability first increases due to hydrate dissociation and then decreases as soil compaction occurs at the later stage of depressurization.

2.3. Importance of K/K_0 for Gas Production by the Depressurization Method

It is argued that the ratio of the permeability sediments after hydrate dissociation to that of the sediments with hydrates (K/K_0) controls the distribution of fluid pressure, considering that the capillary pressure between the water and gas of a sediment much smaller than the magnitude of the pressure decreases at the well. When the radius of the location of the hydrate dissociation front is r^* , the magnitude of the wellbore pressure p_{well} required can be estimated using the following expression [56].

$$P_{well} = p^* - \frac{K_0}{K} \frac{\ln r^* - \ln r_{well}}{\ln r_{far} - \ln r^*} (p_{far} - p^*) \quad (16)$$

where p^* is the phase equilibrium pressure, which is related to temperature; p_{far} denotes the pore pressure at the far-end boundary, which is equal to the initial pressure; r_{well} is the radius of the wellbore and r_{far} denotes the radius of the far-end boundary. Although the permeability varies spatially and temporarily during depressurization, as a conceptual model, it is assumed here that the permeability of the undissociated zone remains K_0 and that of the dissociated zone is K .

The pressure distribution is described using the following equations

$$p = \begin{cases} p^* - \frac{\ln r^* - \ln r}{\ln r_{far} - \ln r^*} (p_{far} - p^*) & \text{when } r^* < r < r_{far} \\ p^* - \frac{K_0}{K} \frac{\ln r^* - \ln r}{\ln r_{far} - \ln r^*} (p_{far} - p^*) & \text{when } r_{well} < r < r^* \end{cases} \quad (17)$$

Figure 3 shows the meaning of the notations in Equation (17). The blue solid line describes the pore-pressure distribution in the formations when considering soil compaction. The red dash line represents the pore-pressure distribution in the formations without the consideration of soil compaction. In the steady state analysis, this distribution is related to the ratio of the permeability of the hydrate-dissociated zone to the permeability of the undissociated zone.

Figure 4 shows the pore-pressure distribution for five different K/K_0 cases (100, 10, 1, 0.5 and 0.1) when the well pressure is reduced to 4.5 Mpa from the initial pore pressure of 13 Mpa. The phase equilibrium pressure that initiates hydrate dissociation is 8.38 Mpa. The lower permeability region dominates the pressure drop and, hence, the hydrate dissociation front is largely dependent on K/K_0 values. When K/K_0 is one, the dissociation front is 6.69 m from the wellbore. When soil compaction is not considered, K/K_0 is often greater than one as hydrate dissociation increases permeability, hence the dissociation front becomes much greater than 6.69 m. However, as shown later, soil compaction can lead to K/K_0 becoming smaller than one for compressible sediment. As shown in the figure, this leads to a reduction in the radius of the dissociation front (0.20 m

for $K/K_0 = 0.5$ and 1.52 m for $K/K_0 = 0.1$). This means a limited volume of gas production because of the soil compaction effect, which has a significant practical implication.

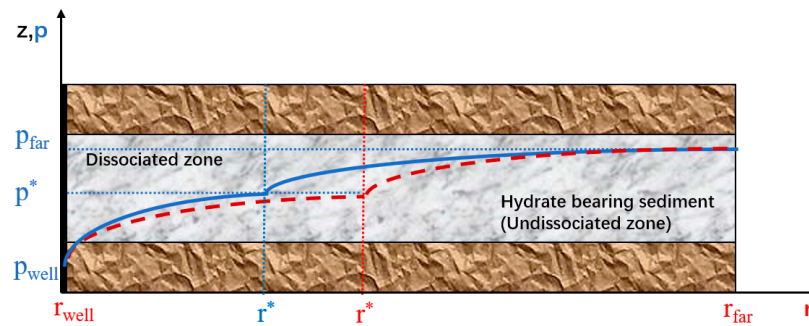


Figure 3. The diagram of pore-pressure distribution in hydrate formations in the case of constant well pressure.

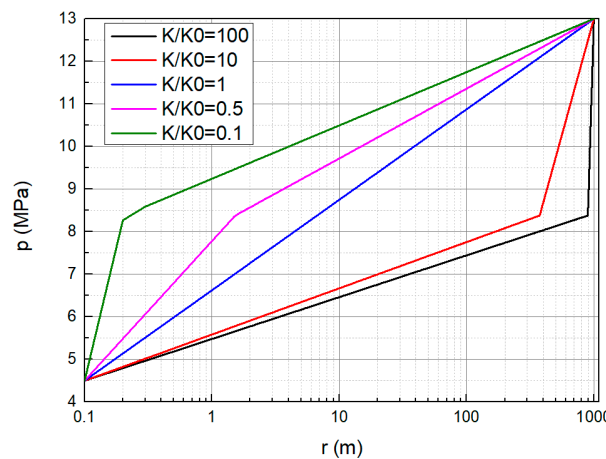


Figure 4. The distribution of pore pressure for constant well pressure.

It is possible to find the ‘critical’ vertical effective stress σ'_{vc} when the permeability becomes smaller than the initial permeability K_0 by making $K = K_0$ in Equation (15).

$$\left(1 + \frac{\kappa_0 \ln\left(\frac{\sigma'_{v0}}{\sigma'_{yi}}\right) - \lambda_0 \ln\left(\frac{\sigma'_v - as_h^b}{\sigma'_{yi}}\right)}{e_0} \right)^\beta \left(\frac{1 - s_h}{1 - s_{h0}} \right)^N = 1 \tag{18}$$

when $\beta > 0$, a critical vertical effective stress σ'_{vc} can be defined from Equation (18) as follows.

$$\sigma'_{vc} = \sigma'_{yi} \exp\left(\frac{e_0 - e_0 \left(\frac{1 - s_{h0}}{1 - s_h} \right)^{\frac{N}{\beta}} + \kappa_0 \ln\left(\frac{\sigma'_{v0}}{\sigma'_{yi}}\right)}{\lambda_0} \right) + as_h^b \tag{19}$$

If the vertical effective stress σ'_v after depressurization is less than σ'_{vc} , there is no permeability reduction compared to the original state.

In this discussion, it is assumed that K is constant within the dissociated zone. However, when the soil compaction effect is considered, permeability will be a function of the effective vertical stress and, hence, K will change spatially and temporally. Such consideration requires a numerical simulation of a thermo-hydro-mechanical coupled model. However, in this study, a simple semi-analytical method to evaluate K/K_0 during the

depressurization process is proposed to conduct a back-of-the-envelope estimation of the effect of the permeability change on gas production by depressurization. The change in K/K_0 during depressurization is modelled by coupling a model that gives a decrease in permeability by an increase in effective vertical stress (as discussed earlier) and a model that computes the transient change in hydrate saturation during depressurization. The latter is presented in the next section.

2.4. Permeability Ratio Changes during the Transient Stage of Dissociation

Hydrate dissociation due to depressurization is a transient process, in which temperature, pressure, water and gas saturation are all associated with hydrate dissociation. The permeability change during the transient stage of dissociation can be evaluated as follows.

The volume change of the host sediment is identical to the change in the pore volume of the sediment by supposing that the particles of the sediments are incompressible. The following equation can be obtained

$$-\frac{dn}{dt} + (1-n)\frac{d\varepsilon_V}{dt} = 0 \quad (20)$$

where n is the porosity of the host sediment, which is related to the void ratio $e = n/(1-n)$. ε_V is the volumetric strain.

The mass conservation equation for hydrate is introduced to calculate the change in hydrate saturation during depressurization.

$$\frac{d(n\rho_h s_h)}{dt} + n\rho_h s_h \frac{d\varepsilon_V}{dt} = \frac{dm_h}{dt} \quad (21)$$

where ρ_h is the hydrate density, and $\frac{dm_h}{dt}$ is the dissociation rate.

Kim et al. [57] proposed a first-order kinetics governing equation to describe the dissociation process, in which the dissociation rate was proportional to the product of the specific surface area and fugacity difference:

$$\frac{dm_h}{dt} = -n \left(s_h A_{hs} K_d M_h \langle p_{eq} - p_g \rangle \right) \quad (22)$$

where M_h is the molar mass of the hydrate, A_{hs} is the specific area, K_d is the hydrate dissociation dynamics coefficient; p_g is the gas pressure at a certain temperature, p_{eq} is the phase equilibrium pressure dependent on this temperature. $\langle \cdot \rangle$ are Macaulay brackets describing the ramp function. N is the porosity of the host sediments. S_h is the hydrate saturation.

The phase equilibrium curve is usually described using a Kamath regression equation [58],

$$p_{eq} = \exp \left(E_1 - \frac{E_2}{T} \right) \quad (23)$$

where E_1 and E_2 are two regression coefficients. In this study, the two coefficients are $E_1 = 39.08$ and $E_2 = 8520$.

According to the experimental results provided by Kim et al. [57], K_d depends on surface activation energy and temperature:

$$K_d = K_{d0} \exp \left(\frac{\Delta E_d}{RT} \right) \quad (24)$$

where $\Delta E_d = -78,300$ J/mol is the surface activation energy of hydrate dissociation, $K_{d0} = 1.24 \cdot 10^5$ mol/(m²·Pa·s), and R is the ideal gas constant.

Substituting Equations (23) and (24) into Equation (22), we obtain

$$\frac{d(n\rho_h s_h)}{dt} + \frac{n}{1-n} \rho_h s_h \frac{dn}{dt} = -n \left(s_h A_{hs} K_{d0} M_h < \exp\left(E_1 + \frac{\Delta E_d - E_2 R}{RT}\right) - p_g \exp\left(\frac{\Delta E_d}{RT}\right) > \right) \quad (25)$$

As $n = \frac{e}{1+e}$ and supposing ρ_h is a constant, Equation (25) becomes

$$\rho_h \frac{e}{1+e} \frac{ds_h}{dt} + \frac{1}{1+e} \rho_h s_h \frac{de}{dt} = -\frac{e}{1+e} \left(s_h A_{hs} K_{d0} M_h < \exp\left(E_1 + \frac{\Delta E_d - E_2 R}{RT}\right) - p_g \exp\left(\frac{\Delta E_d}{RT}\right) > \right) \quad (26)$$

After simplification,

$$\frac{1}{e s_h} \frac{d(es_h)}{dt} = -\frac{A_{hs} K_{d0} M_h}{\rho_h} < \exp\left(E_1 + \frac{\Delta E_d - E_2 R}{RT}\right) - p_g \exp\left(\frac{\Delta E_d}{RT}\right) > \quad (27)$$

This equation can be integrated as follows.

$$\ln\left(\frac{es_h}{e_0 s_{h0}}\right) = -\frac{A_{hs} K_{d0} M_h}{\rho_h} \int_{t_0}^t < \exp\left(E_1 + \frac{\Delta E_d - E_2 R}{RT(t)}\right) - p_g(t) \exp\left(\frac{\Delta E_d}{RT(t)}\right) > dt \quad (28)$$

Substituting Equation (12) into Equation (28) becomes,

$$s_h(t) = \frac{e_0 s_{h0} \exp\left(-\frac{A_{hs} K_{d0} M_h}{\rho_h} \int_{t_0}^t < \exp\left(E_1 + \frac{\Delta E_d - E_2 R}{RT(t)}\right) - p_g(t) \exp\left(\frac{\Delta E_d}{RT(t)}\right) > dt\right)}{e_0 + \kappa_0 \ln \sigma'_{v0} - \lambda_0 \ln(\sigma'_v - a s_h^b) + (\lambda_0 - \kappa_0) \ln \sigma'_{yi}} \quad (29)$$

Equation (29) can be used to evaluate the change in hydrate saturation with time. However, this equation is a highly nonlinear and there is no explicit expression of s_h . In this study, an iteration method is used to evaluate the time dependent changes in s_h .

Assuming that the gas may be released instantly after hydrate dissociation, the total vertical stress σ_{v0} remains constant and the capillary pressure is negligible ($p_g = p_w = p_p$, where p_p denotes pore pressure). Equation (13) describes the permeability change during depressurization and can be rewritten as follows.

$$K(t) = K_{s0} \left(1 + \frac{\kappa_0 \ln\left(\frac{\sigma'_{y0}}{\sigma'_{yi}}\right) - \lambda_0 \ln\left(\frac{\sigma_{v0} - p_p(t) - a s_h(t)^b}{\sigma'_{yi}}\right)}{e_0} \right)^\beta (1 - s_h(t))^N \quad (30)$$

where $s_h(t)$ is obtained using Equation (28).

From Equation (30), the variation of permeability with time is dependent not only on the state of pore pressure but also on the history of both temperature and pore pressure. Equations (28) and (29) provide a method for estimating the change in the effective permeability of the HBS with time through the time series of pore pressure and temperature considering hydrate dissociation and soil compaction.

3. Parametric Study and Results

As shown by Equation (30), there are eight parameters that relate compaction and hydrate dissociation to permeability. The initial intrinsic permeability of the host sediment K_{s0} is set to be 100 millidarcies. The initial porosity n_0 is 0.418. The parameters a and b equal 20.1 and 1, respectively, provided by Uchida et al. [53]. Different values of initial hydrate saturation s_{h0} (0, 0.4 and 0.8) are chosen in the range of the real test data obtained from HBS samples obtained from the Nankai Trough site [53].

In the parametric study, the initial vertical effective stress is set to be 3 Mpa, whereas the initial water pressure is 13 Mpa. The total vertical stress (16 Mpa) is kept constant during depressurization. The water pressure decreases from 13 Mpa to 3 Mpa over ten

hours and, hence, the vertical effective stress increases from 3 Mpa to 13 Mpa. The rate of depressurization is set according to the rate of depressurization in the Nankai Trough production [59]. Based on Equation (23), the phase equilibrium pressure is 8.38 Mpa at an initial temperature of 283.56 K.

The parameters used for the parametric study are shown in Table 1. The hydrate permeability parameter N is related to the hydrate morphology in the pores. For bonding or coating morphology, N is about 2, whereas for pore-filling morphology, N is about 6 [52]. Ren et al. [51] show that the compaction–permeability parameter β ranges between 2 and 6. When β equals zero, the effect of compaction on permeability is ignored. According to the triaxial test data from the Nankai HBS specimens, the parameter $\lambda = 0.15$ and $\kappa = 0.01$ [53]. The range of the values of these two parameters is, therefore, given as listed in Table 1.

Table 1. Parameters and Initial Conditions.

Parameters	s_{h0}	N	β	λ	κ	σ'_{yi}
Variations	0, 0.4, 0.8	2, 4, 6	0, 4, 7, 10	0.1, 0.15, 0.2	0.005, 0.01, 0.015	2, 3, 4 Mpa

Two scenarios are considered in this study. The first scenario assumes a constant temperature condition, in which the heat supply during hydrate dissociation is large enough to keep the temperature at 283.56 K. The endothermic process is, therefore, ignored and the phase equilibrium pressure remains constant during hydrate dissociation. The second scenario considers the heat-insulation condition. The endothermic process is considered, but there is no heat conduction from the outside. The temperature decreases and then hydrate dissociation stops at a certain point, resulting in residual hydrate. In reality, the supply of heat is made by both conduction and convection and, hence, the two scenarios are considered to be the two extreme situations.

3.1. Scenario 1 Constant Temperature Case

In this scenario, the temperature remains at its initial value $T_0 = 283.56$ K. The hydrate dissociates when the pressure becomes equal to the phase equilibrium pressure of 8.38 Mpa at this given temperature. Figure 5a shows the changes in permeability, whereas Figure 5b shows the changes in the permeability ratio. Three different initial hydrate saturations ($s_h = 0, 0.4$ and 0.8) are considered. The model parameters are $N = 4$, $\beta = 7$, $\lambda = 0.15$, $\kappa = 0.01$ and $\sigma'_y = 3$ Mpa (normally consolidated). Results are shown for the cases with and without the soil compaction effect.

The Initial hydrate saturation prior to depressurization determines the Initial permeability. The changes in permeability can be separated into three phases: (i) before hydrate dissociation (Phase I), (ii) during hydrate dissociation (Phase II) and (iii) after hydrate dissociation (Phase III). In Phase I, there is no hydrate dissociation and the permeability decreases by volumetric compression for all three initial hydrate saturation cases ($s_h = 0, 0.4$ and 0.8). In Phase II, the water pressure becomes smaller than the phase equilibrium pressure, hydrate dissociation creates pore space and the effective permeability increases. For the high initial hydrate saturation case ($s_h = 0.8$), there is a large permeability increase due to hydrate dissociation. In Phase III, hydrate is dissociated completely. The permeability values of the three different hydrate saturation cases become the same. In this phase, the reduction in permeability becomes important due to soil compaction by further depressurization. If the soil compaction effect is not considered, the permeability ratio K/K_0 is always greater than one. When the soil compaction effect is considered, however, the permeability ratio K/K_0 becomes less than one at the end of depressurization for the medium hydrate saturation case ($s_h = 0.4$). For the high hydrate saturation case ($s_h = 0.8$), K/K_0 remains greater than one, even with the soil compaction effect considered because of the significant increase in permeability due to hydrate dissociation. Hence, it is the medium hydrate saturation condition that can have a noticeable soil compaction effect on gas production.

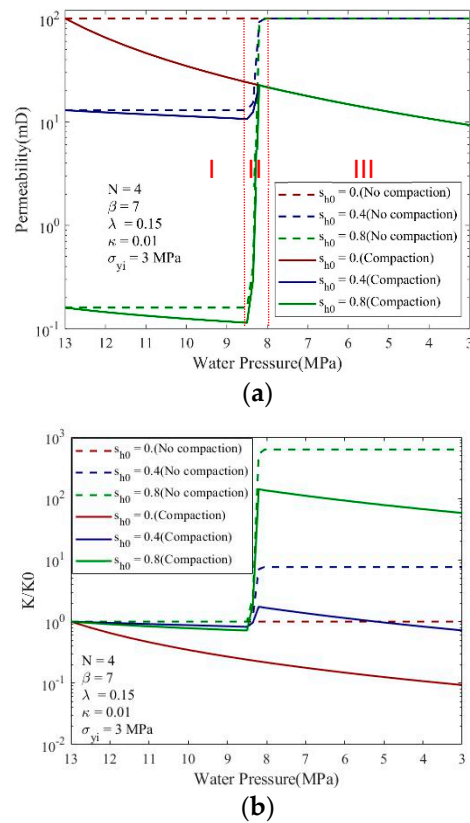


Figure 5. Variation of (a) effective permeability and (b) permeability ratio of HBSs with depressurization corresponding to different initial hydrate saturations.

Figure 6 shows the effect of N , which controls the change in permeability with hydrate saturation. The initial hydrate saturation is fixed at $s_h = 0.4$. The initial permeability decreases with an increase in parameter N . A smaller value of N ($N = 2$ in this case) implies less permeability change during depressurization, as shown by the lines of the no-soil-compaction effect. It is this case that soil compaction reduces permeability significantly and the permeability ratio K/K_0 becomes around 0.25 (see Figure 6b). Gas production would be affected by soil compaction in this case.

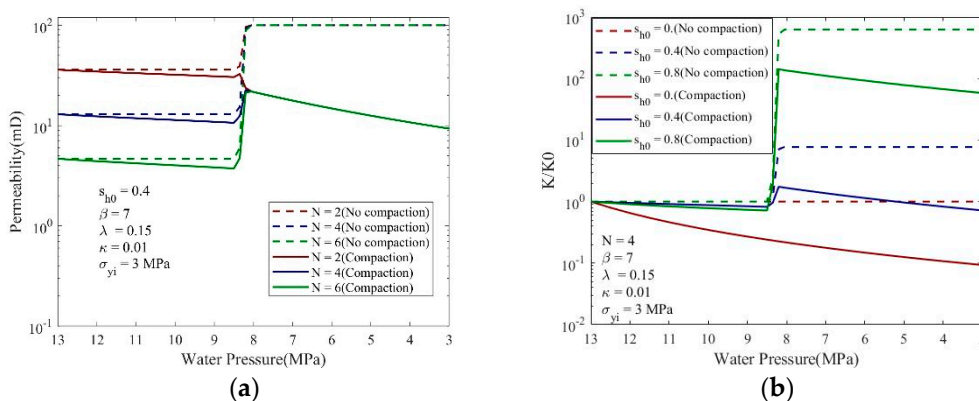


Figure 6. The effect of parameter N on (a) permeability and (b) permeability ratio.

Figure 7 shows the effect of parameter β on permeability change. A large β value implies a large soil compaction effect on permeability, as shown by a larger decreasing rate as the depressurization continues. The ratio K/K_0 becomes smaller than one when β is greater than 7, as shown in Figure 7b. Figure 8 shows the permeability ratio K/K_0 after depressurization ($p_w = 3$ MPa) for different initial hydrate saturation cases. The four

figures correspond to four different N value cases. Each figure shows the effect of β for a given N value. For the compression parameters considered ($\lambda = 0.15$, $\kappa = 0.01$, $\sigma'_{yi} = 3$ MPa, $\beta > 4$), the effective permeability ($p_w = 3$ MPa) becomes less than the initial permeability when the initial hydrate saturation is less than 0.5 and N is equal to 2.

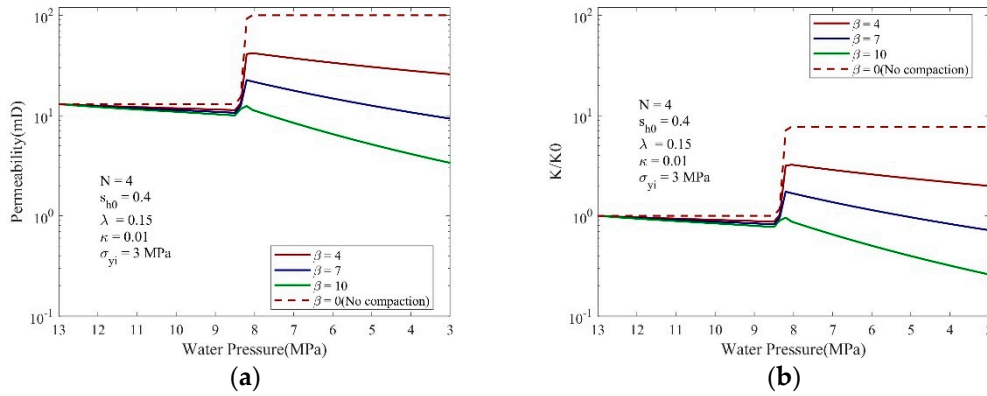


Figure 7. The effect of parameter β on (a) permeability and (b) permeability ratio.

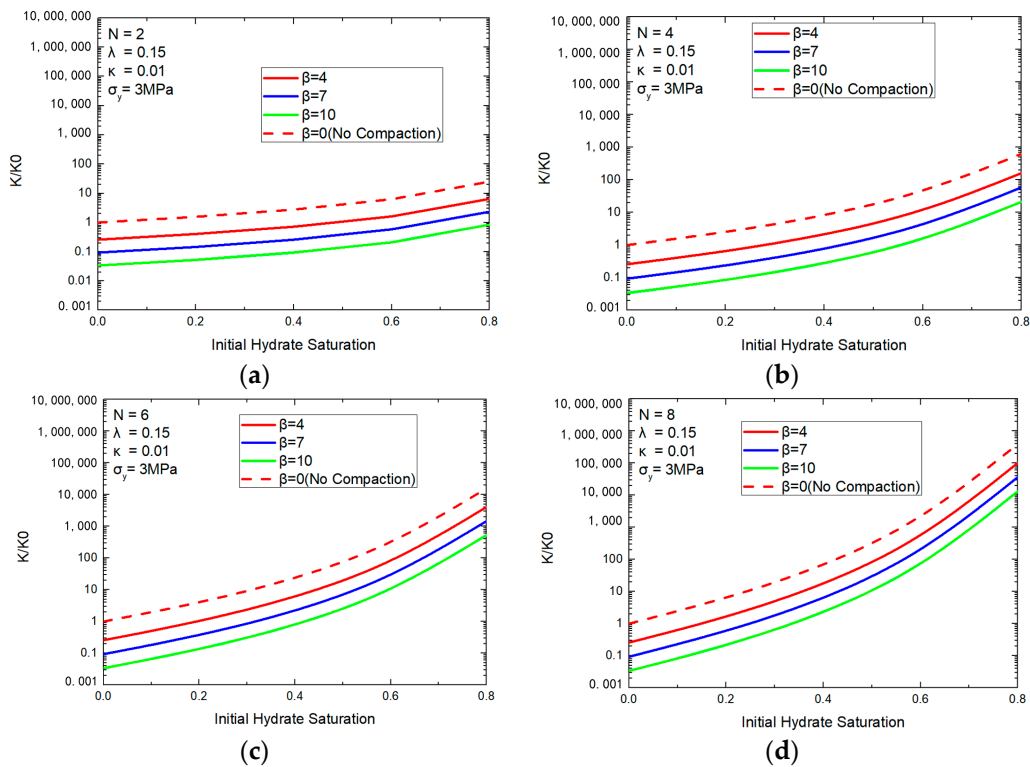


Figure 8. The effect of parameter β on the relationship between permeability ratio K/K_0 and initial hydrate saturation when (a) $N = 2$, (b) $N = 4$, (c) $N = 6$ and (d) $N = 8$ in the case of constant temperature.

Apart from parameter β , the magnitude of the compaction is governed by three soil deformation parameters describing the compressive behavior of HBSs. These include compressive coefficient λ , swelling coefficient κ , and preconsolidation pressure σ'_{yi} . Figure 9a shows how parameter λ affects the change in permeability during depressurization for the cases with their other parameters fixed. The permeability decreases with depressurization when parameter λ equals 0.2, but increases when λ equals 0.1. The higher the value of λ , the larger the volume contraction becomes, resulting in lower permeability. Figure 9b shows that the elastic stiffness parameter κ has a relatively weak influence during Phase I than the other two phases. After sediment yielding (i.e., effective vertical

stress becoming greater than the yield stress), the magnitude of permeability is dominated by plastic compression and, hence, the effect of κ becomes small. Figure 9c shows that the permeability increases with the yield stress σ'_{yi} when the initial vertical effective stress is 3 MPa. When $\sigma'_{yi} < 3$ MPa, the host sediment is in the underconsolidated state and hence the sediment compacts rapidly as the hydrate starts to dissociate. When $\sigma'_{yi} > 3$ MPa, the host sediment is in the overconsolidated state and, hence, the permeability does not decrease to the level of the normally consolidated case with the same compression parameters.

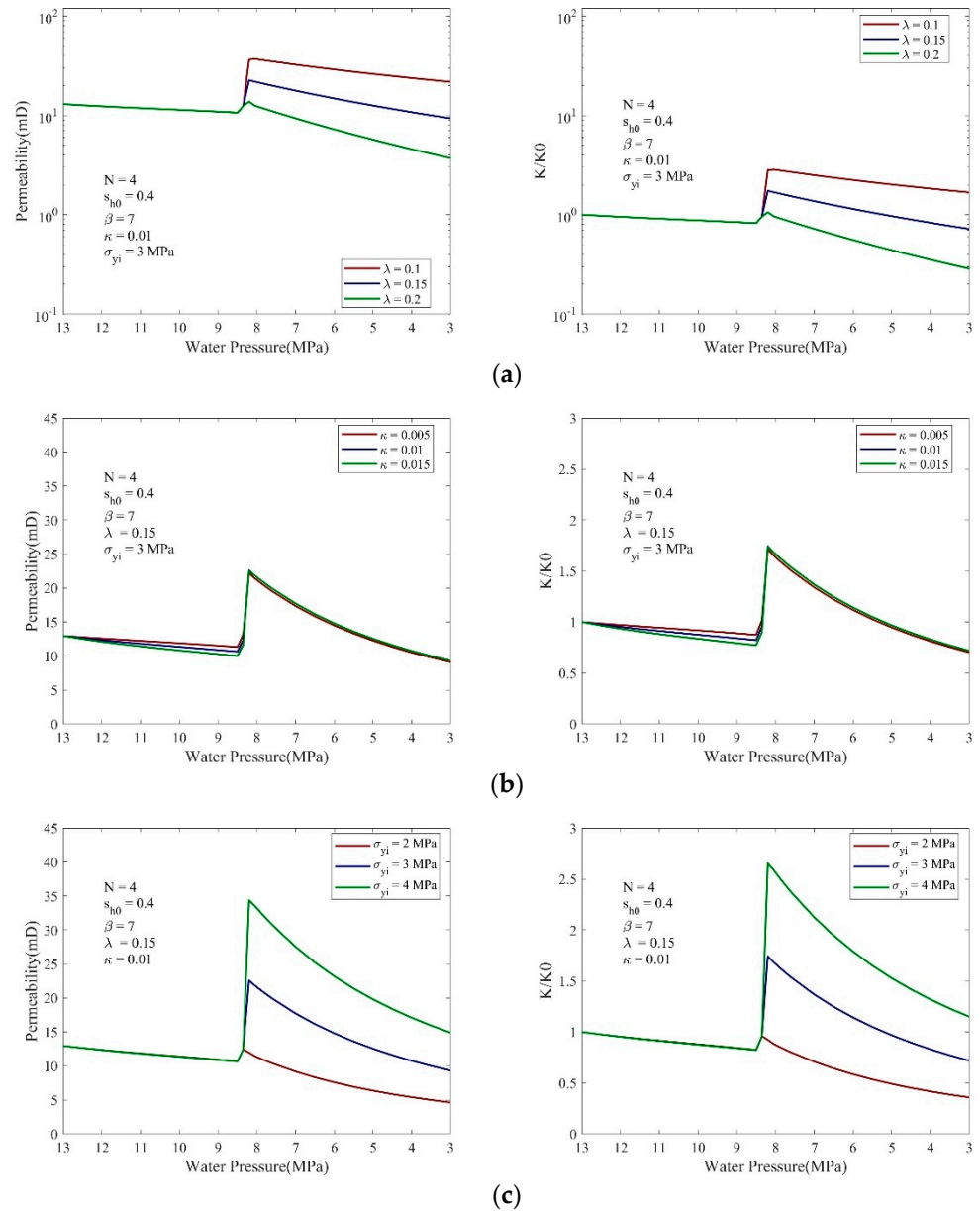


Figure 9. The impact of different parameters including (a) parameter λ , (b) parameter κ and (c) pre-condition pressure σ_y on permeability (Left figures—permeability, Right figures—permeability ratio).

3.2. Scenario 2 Heat-Insulated Case

In the heat insulation condition, the temperature decreases with hydrate dissociation because hydrate dissociation is an endothermal process, and it is assumed that there is no heat supply during depressurization. Because of this, the hydrate will not fully dissociate and some residual hydrate will be left for a given depressurization value. In a real gas

production condition, there is neither absolute heat insulation (as in this case) nor constant temperature (as discussed earlier). The actual condition should be in a range between the two limits.

In this scenario, the Kamath equation [58] is used to compute the absorbed heat ΔH from the system stored heat during the dissociation [57].

$$\Delta H = 56599 - 16.744T \quad (31)$$

$$C_T \frac{dT}{dt} = -n \Delta H \left(s_h A_{hs} K_d M_h < P_{eq} - p_g > \right) \quad (32)$$

where the heat capacity of HBSs $C_T = 2.31 \times 10^6 \text{ J/m}^3/\text{K}$, dissociation kinetic coefficient $K_d = 123 \times 10^3 e^{\frac{9.42 \times 10^3}{T}}$ and specific area $A_{hs} = 0.3 \frac{1}{\mu\text{m}}$.

As before, a higher initial hydrate saturation corresponds to lower initial effective permeability. During hydrate dissociation, effective permeability increases at the beginning. As there is no heat supply from outside, the water pressure decreases along the phase equilibrium curve, as shown in Figure 10a, which is the self-preservation phenomenon of hydrate. As a result, the hydrate dissociation rate is much smaller than that in the previous case and there will be residual hydrate saturation after the target pressure of 3 MPa is reached, as shown in Figure 10b. As the dissociation occurs, the effective vertical stress increases and, hence, soil compaction occurs. The permeability then decreases. As shown in Figure 11, the soil compaction effect is more apparent in low initial hydrate saturation cases. For the cases with high initial hydrate saturations, the effective permeability is mainly affected by hydrate dissociation.

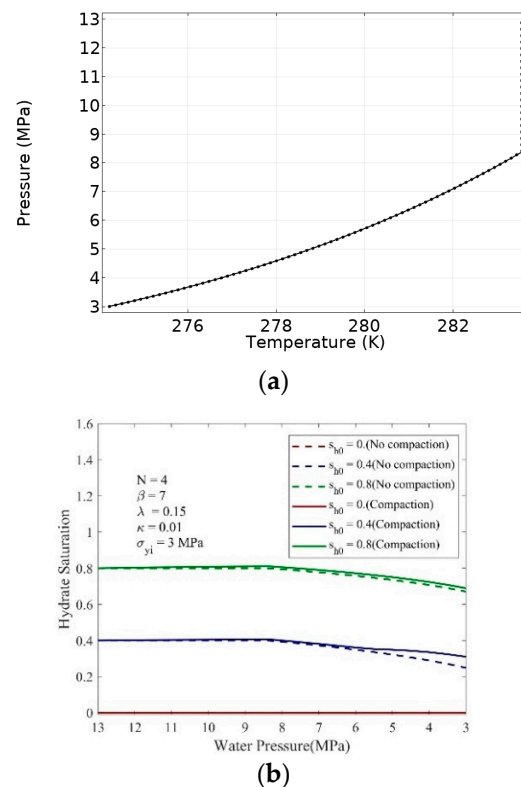


Figure 10. The variation of the (a) P–T path and (b) hydrate saturation during hydrate dissociation.

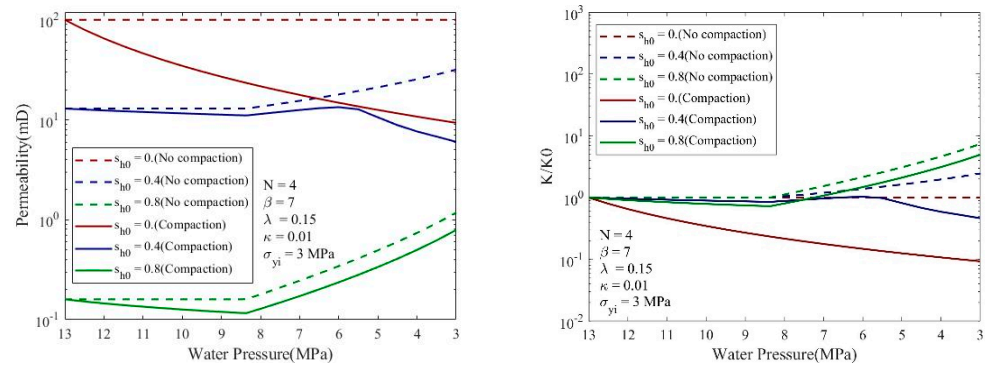


Figure 11. The vibration of effective permeability of HBSs with depressurization corresponding to different initial hydrate saturation (Left figures—permeability, Right figures—permeability ratio).

Figure 12 shows that the effect of parameters N and β on the permeability ratio changes. The soil compaction effect becomes apparent when the N value decreases and the β value increases. Unlike the previous scenario, the effective permeability under the heat-insulated condition increases slightly at the beginning of hydrate dissociation, then decreases with compaction; this is because hydrate dissociates little, and the compaction governs the decrease in permeability. All cases show K/K_0 becoming less than one at the end of depressurization.

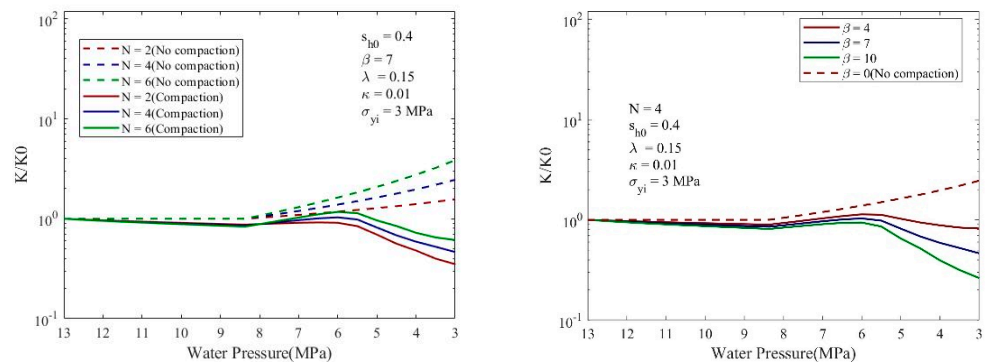


Figure 12. The effect of parameters N and β on permeability ratio K/K_0 (Left figures— N , Right figures— β).

The plots of the ratio of effective permeability after depressurization ($p_w = 3$ MPa) to the initial effective permeability (K/K_0) for the insulated scenario are given in Figure 13. Each plot shows the effect of β for a given N value. For the compression parameters considered ($\lambda = 0.15$, $\kappa = 0.01$, $\sigma'_y = 3$ MPa, $\beta > 4$), the permeability ($p_w = 3$ MPa) becomes less than the initial permeability when the initial hydrate saturation is less than 0.416 and N is less than 4. The soil compaction effect on permeability becomes more apparent in this insulated scenario than in the constant temperature scenario. This is because hydrate does not dissociate fully, so the permeability does not change much but the sediment compresses due to a reduction in pressure.

The effects of the soil deformation parameters (λ , κ and σ'_{yi}) on the permeability ratio K/K_0 are shown in Figure 14. As the sediment becomes softer (large values of λ , κ and a smaller value of σ'_{yi}), the soil compaction effect on permeability is greater and the K/K_0 values reduce. Again, the soil compaction effect becomes more apparent in the insulated scenario compared with the constant temperature scenario, indicating the importance of heat transfer to dissociate hydrate fully.

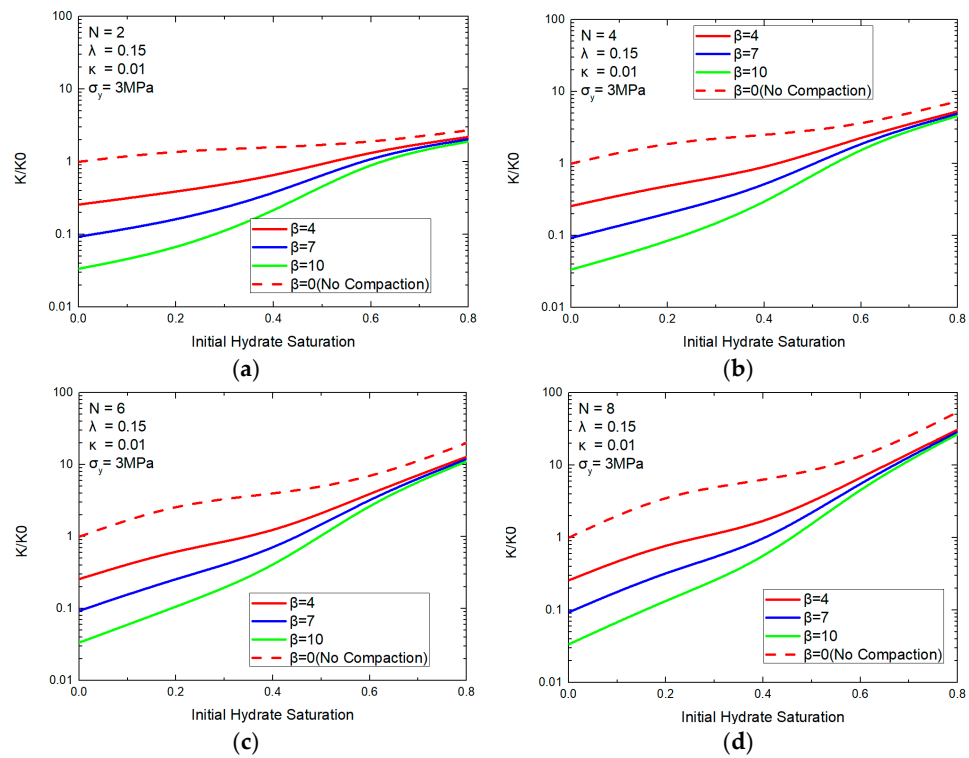


Figure 13. The effect of parameter β on the relationship between permeability ratio K/K_0 and initial hydrate saturation when (a) $N = 2$, (b) $N = 4$, (c) $N = 6$ (d) $N = 8$ in the case of heat insulation.

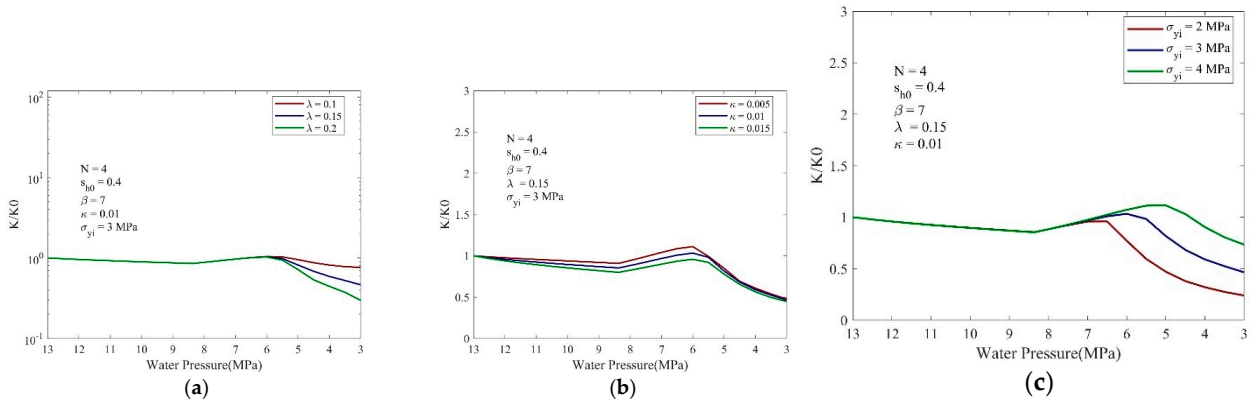


Figure 14. The impact of different parameters on permeability ratio K/K_0 included in the scenario of heat insulation (a) parameter λ , (b) parameter κ and (c) precondition pressure σ'_y .

4. Conclusions

The study described in this paper analyzes the change in permeability during depressurization considering the volume contraction due to the increase in effective stress and the degradation of the bonded structure. Combining three models (hydrate-saturation dependent permeability model, permeability–void ratio model, and hydrate soil compaction model), a semi-analytic method to evaluate permeability change through pore pressure and temperature during depressurization is proposed. The method enables the evaluation of the ratio of the effective permeability after depressurization to the initial effective permeability (K/K_0), which is important in evaluating the extent of dissociation in the HBS from the depressurized wellbore location. A parametric study was conducted to show the effects of model parameters on the change in permeability based on two scenarios (constant temperature and heat insulated).

Results of the parametric study show the relative effects of soil compaction and hydrate dissociation on permeability change by the depressurization method. A typical magnitude of depressurization in the field is in the order of 10 MPa, which in turn increases the effective stress of the sediment by a similar magnitude. If the soil compaction effect is not considered, the pressure drawdown in the hydrate reservoir occurs mainly in the undissociated zone because of the increase in permeability due to hydrate dissociation. However, when soil compaction is considered, the ratio of K/K_0 does not increase much or, in certain cases, the ratio becomes less than one, especially in the heat-insulated scenario when the hydrate does not dissociate fully. In such a case, the extent of dissociation becomes limited compared with the case when soil compaction is not considered, and this has practical implications on gas production by depressurization.

The method proposed in this paper allows a simple back-of-the-envelope evaluation of the soil compaction effect on permeability change when the depressurization method is used for gas production from HBSs. If the effect is evaluated as being critical for gas production evaluation, then the next step can be to perform a fully coupled thermo-hydro-mechanical simulation for estimating the spatial and temporal variations in the pressure field in the HBSs and the gas/water production rate, which can be affected by the soil compaction effect.

Author Contributions: Conceptualization, X.S. and K.S.; methodology, X.S.; resources, X.S.; data curation, H.L.; writing—original draft preparation, X.S. and H.L.; writing—review and editing, K.S.; funding acquisition, X.S. and K.S. All authors have read and agreed to the published version of the manuscript.

Funding: National Natural Science Foundation of China: 51909025.

Institutional Review Board Statement: Not applicable.

Informed Consent Statement: Not applicable.

Data Availability Statement: Not applicable.

Conflicts of Interest: The authors declare no conflict of interest. The funders had no role in the design of the study; in the collection, analyses, or interpretation of data; in the writing of the manuscript; or in the decision to publish the results.

References

1. Demirbas, A. Methane hydrates as potential energy resource: Part 1—Importance, resource and recovery facilities. *Energy Convers. Manag.* **2010**, *51*, 1547–1561. [[CrossRef](#)]
2. Dvorkin, J.; Prasad, M.; Sakai, A.; Lavoie, D. Elasticity of marine sediments: Rock physics modeling. *Geophys. Res. Lett.* **1999**, *26*, 1781–1784. [[CrossRef](#)]
3. Hyodo, M.; Li, Y.; Yoneda, J.; Nakata, Y.; Yoshimoto, N.; Nishimura, A. Effects of dissociation on the shear strength and deformation behavior of methane hydrate-bearing sediments. *Mar. Pet. Geol.* **2014**, *51*, 52–62. [[CrossRef](#)]
4. Li, Y.; Song, Y.; Liu, W.; Yu, F.; Wang, R. A new strength criterion and constitutive model of gas hydrate-bearing sediments under high confining pressures. *J. Pet. Sci. Eng.* **2013**, *109*, 45–50. [[CrossRef](#)]
5. Suzuki, K.; Schultheiss, P.; Nakatsuka, Y.; Ito, T.; Egawa, K.; Holland, M.; Yamamoto, K. Physical properties and sedimentological features of hydrate-bearing samples recovered from the first gas hydrate production test site on Daini-Atsumi Knoll around eastern Nankai Trough. *Mar. Pet. Geol.* **2015**, *66*, 346–357. [[CrossRef](#)]
6. Freij, R.; Tan, C.; Clennell, B.; Tohidi, B.; Yang, J. A wellbore stability model for hydrate bearing sediments. *J. Pet. Sci. Eng.* **2007**, *57*, 209–220. [[CrossRef](#)]
7. Nixon, M.F.; Grozic, J.L.H. Submarine slope failure due to gas hydrate dissociation: A preliminary quantification. *Can. Geotech. J.* **2007**, *44*, 314–325. [[CrossRef](#)]
8. Konno, Y.; Fujii, T.; Sato, A.; Akamine, K.; Naiki, M.; Masuda, Y.; Yamamoto, K.; Nagao, J. Key findings of the world's first off shore methane hydrate production test off the coast of Japan: Toward future commercial production. *Energy Fuels* **2017**, *31*, 2607–2616. [[CrossRef](#)]
9. Li, J.; Ye, J.; Qin, X.; Qiu, H.; Wu, N.; Lu, H.; Xie, W.; Lu, J.; Peng, F.; Xu, Z.; et al. The first offshore natural gas hydrate production test in South China Sea. *China Geol.* **2018**, *1*, 5–16. [[CrossRef](#)]
10. Jang, J.; Santamarina, J.C. Evolution of gas saturation and relative permeability during gas production from hydrate-bearing sediments: Gas invasion vs. gas nucleation. *J. Geophys. Res. Solid Earth* **2014**, *119*, 116–126. [[CrossRef](#)]

11. Wang, B.; Fan, Z.; Zhao, J.; Lv, X.; Pang, W.; Li, Q. Influence of intrinsic permeability of reservoir rocks on gas recovery from hydrate deposits via a combined depressurization and thermal stimulation approach. *Appl. Energy* **2018**, *229*, 858–871. [[CrossRef](#)]
12. Masuda, Y.; Fujinaga, Y.; Naganawa, S.; Fujita, K.; Sato, K.; Hayashi, Y. Modeling and experimental studies on dissociation of methane gas hydrates in Berea sandstone cores. In Proceedings of the Third International Gas Hydrate Conference, Salt Lake City, UT, USA, 18–22 July 1999.
13. Minagawa, H.; Ohmura, R.; Kamata, Y.; Ebinuma, T.; Narita, H.; Masuda, Y. Water permeability measurements of gas hydrate-bearing sediments. In Proceedings of the 5th International Conference on Gas Hydrates, Trondheim, Norway, 13–16 June 2005.
14. Nimblett, J.; Ruppel, C. Permeability evolution during the formation of gas hydrates in marine sediments. *J. Geophys. Res. Solid Earth* **2003**, *108*, 1–17. [[CrossRef](#)]
15. Kumar, A.; Maini, B.; Bishnoi, P.; Clarke, M.; Zatsepina, O.; Srinivasan, S. Experimental determination of permeability in the presence of hydrates and its effect on the dissociation characteristics of gas hydrates in porous media. *J. Pet. Sci. Eng.* **2010**, *70*, 114–122. [[CrossRef](#)]
16. Delli, M.; Grozic, J. Prediction Performance of Permeability Models in Gas Hydrate Bearing Sands. In Proceedings of the Canadian Unconventional Resources Conference, Calgary, AB, Canada, 15–17 November 2011.
17. Liang, H.; Song, Y.; Liu, Y.; Yang, M.; Huang, X. Study of the permeability characteristics of porous media with methane hydrate by pore network model. *J. Nat. Gas Chem.* **2010**, *19*, 255–260. [[CrossRef](#)]
18. Katagiri, J.; Konno, Y.; Yoneda, J.; Tenma, N. Pore-scale modeling of flow in particle packs containing grain-coating and pore-filling hydrates: Verification of a Kozeny e Carman-based permeability reduction model. *J. Nat. Gas Sci. Eng.* **2017**, *45*, 537–551. [[CrossRef](#)]
19. Kossel, E.; Deusner, C.; Bigalke, N.; Haeckel, M. The Dependence of water permeability in Quartz sand on gas hydrate saturation in the pore space. *J. Geophys. Res. Solid Earth* **2018**, *123*, 1235–1251. [[CrossRef](#)]
20. Johnson, A.; Patil, S.; Dandekar, A. Experimental investigation of gas-water relative permeability for gas-hydrate-bearing sediments from the Mount Elbert Gas Hydrate Stratigraphic Test Well, Alaska North Slope. *Mar. Pet. Geol.* **2011**, *28*, 419–426. [[CrossRef](#)]
21. Kneafsey, T.; Berkeley, L.; National, Y. Permeability of Laboratory-Formed Methane-Hydrate-Bearing Sand: Measurements and Observations Using X-ray Computed Tomography. *SPE J.* **2004**, *16*, 78–94. [[CrossRef](#)]
22. Jiang, L.; Liu, Y.; Teng, Y.; Zhao, J.; Zhang, Y.; Yang, M.; Song, Y. Permeability estimation of porous media by using an improved capillary bundle model based on micro-CT derived pore geometries. *Heat Mass Transf.* **2017**, *53*, 49–58. [[CrossRef](#)]
23. Liu, W.; Wu, Z.; Li, Y.; Song, Y.; Ling, Z.; Zhao, J.; Lv, Q. Experimental study on the gas phase permeability of methane hydrate-bearing clayey sediments. *J. Nat. Gas Sci. Eng.* **2016**, *36*, 378–384. [[CrossRef](#)]
24. Daigle, H. Relative permeability to water or gas in the presence of hydrates in porous media from critical path analysis. *J. Pet. Sci. Eng.* **2016**, *146*, 526–535. [[CrossRef](#)]
25. Li, G.; Wu, D.; Li, X.; Lv, Q.; Li, C.; Zhang, Y. Experimental measurement and mathematical model of permeability with methane hydrate in quartz sands. *Appl. Energy* **2017**, *202*, 282–292. [[CrossRef](#)]
26. Xu, J.; Bu, Z.; Li, H.; Li, S.; Sun, B. Pore-scale flow simulation on the permeability in hydrate-bearing sediments. *Fuel* **2022**, *312*, 122681. [[CrossRef](#)]
27. Lei, X.; Yao, Y.; Luo, W.; Wen, Z. Permeability change in hydrate bearing sediments as a function of hydrate saturation: A theoretical and experimental study. *J. Pet. Sci. Eng.* **2022**, *208*, 109449. [[CrossRef](#)]
28. Liu, X.; Dong, H.; Yan, W.; Arif, M.; Zhang, Y.; Golsanami, N. Influence of gas hydrate saturation and pore habits on gas relative permeability in gas hydrate-bearing sediments: Theory, experiment and case study. *J. Nat. Gas Sci. Eng.* **2021**, *95*, 104171. [[CrossRef](#)]
29. Hu, C.; Jia, Y.; Duan, Z. The influence of inhomogeneous hydrate formation on permeability anisotropy of porous media. *Geo-Mar. Lett.* **2021**, *41*, 10. [[CrossRef](#)]
30. Hu, C.; Jia, Y.; Duan, Z. Pore scale study of the permeability anisotropy of sands containing grain-coating and pore-filling hydrates. *J. Pet. Sci. Eng.* **2022**, *215*, 110590. [[CrossRef](#)]
31. Wu, Z.; Yang, S.; Liu, W.; Li, Y. Permeability analysis of gas hydrate-bearing sand/clay mixed sediments using effective stress laws. *J. Nat. Gas Sci. Eng.* **2022**, *97*, 104376. [[CrossRef](#)]
32. Liu, W.; Wu, Z.; Li, J.; Zheng, J.; Li, Y. The seepage characteristics of methane hydrate-bearing clayey sediments under various pressure gradients. *Energy* **2020**, *191*, 116507. [[CrossRef](#)]
33. Zhou, S.; Li, M.; Wu, P.; Liu, Y.; Zhang, L.; Yang, L.; Li, Y.; Zhao, J.; Song, Y. Permeability analysis of hydrate-bearing porous media considering the effect of phase transition and mechanical strain during the shear process. *SPE J.* **2022**, *27*, 422–433. [[CrossRef](#)]
34. Zhou, S.; Wu, P.; Li, M.; Li, Y.; Zhang, L.; Yang, L.; Liu, Y.; Zhao, J.; Song, Y. Effect of hydrate dissociation and axial strain on the permeability of hydrate-bearing sand during the creep process. *SPE J.* **2021**, *26*, 2837–2848. [[CrossRef](#)]
35. Wu, P.; Li, Y.; Liu, W.; Liu, Y.; Wang, D.; Song, Y. Microstructure evolution of hydrate-bearing sands during thermal dissociation and ensued impacts on the mechanical and seepage characteristics. *J. Geophys. Res. Solid Earth* **2020**, *125*, e2019JB019103. [[CrossRef](#)]
36. Kuang, Y.; Zhang, L.; Song, Y.; Yang, L.; Zhao, J. Quantitative determination of pore-structure change and permeability estimation under hydrate phase transition by NMR. *AIChE J.* **2020**, *66*, 16859. [[CrossRef](#)]

37. Rutqvist, J.; Moridis, G.; Grover, T.; Silpngarmert, S.; Collett, T.; Holdich, S. Coupled multiphase fluid flow and wellbore stability analysis associated with gas production from oceanic hydrate-bearing sediments. *J. Pet. Sci. Eng.* **2012**, *92*, 65–81. [[CrossRef](#)]
38. Sakamoto, Y.; Kakumoto, M.; Miyazaki, K.; Tenma, N.; Komai, T.; Yamaguchi, T.; Shimokawara, M.; Ohga, K. Numerical study on dissociation of methane hydrate and gas production behavior in laboratory-scale experiments for Depressurization: Part 3-numerical study on estimation of permeability in methane hydrate reservoir. *Int. J. Offshore Polar Eng.* **2009**, *19*, 124–134.
39. Chen, B.; Sun, H.; Zhou, H.; Yang, M.; Wang, D. Effects of pressure and sea water flow on natural gas hydrate production characteristics in marine sediment. *Appl. Energy* **2019**, *238*, 274–283. [[CrossRef](#)]
40. Gupta, S.; Deusner, C.; Haeckel, M.; Helmig, R.; Wohlmuth, B. Testing a coupled hydro-thermo-chemo-geomechanical model for gas hydrate bearing sediments using triaxial compression lab experiments. *Geochem. Geophys. Geosyst.* **2017**, *18*, 3419–3437. [[CrossRef](#)]
41. Rockhold, M.L.; Yarwood, R.; Niemet, M.; Bottomley, P.; Selker, J. Considerations for modeling bacterial-induced changes in hydraulic properties of variably saturated porous media. *Adv. Water Resour.* **2002**, *25*, 477–495. [[CrossRef](#)]
42. Faruk, C. Predictability of Porosity and Permeability Alterations by Geochemical and Geomechanical Rock and Fluid Interactions. In Proceedings of the SPE International Symposium on Formation Damage Control, Lafayette, LA, USA, 23–24 February 2000.
43. Myshakin, E.; Seol, Y.; Lin, J.; Uchida, S.; Collett, T.; Boswell, R. Numerical simulations of depressurization-induced gas production from an interbedded turbidite gas hydrate-bearing sedimentary section in the offshore India: Site NGHP-02-16 (Area-B). *Mar. Pet. Geol.* **2019**, *108*, 619–638. [[CrossRef](#)]
44. Moridis, G.; Reagan, M.; Queiruga, A. Analysis of the flow, thermal and geomechanical behavior of offshore hydrate deposits at the NGHP-02-09-A site during short- and long-term gas production scenarios. *Am. Geophys. Union Fall Meet.* **2017**, *2017*, OS53B-1183.
45. Yoneda, J.; Oshima, M.; Kida, M.; Kato, A.; Konno, Y.; Jin, Y.; Jang, J.; Waite, W.F.; Kumar, P.; Tenma, N. Permeability variation and anisotropy of gas hydrate-bearing pressure-core sediments recovered from the Krishna–Godavari Basin, offshore India. *Mar. Pet. Geol.* **2019**, *108*, 524–536. [[CrossRef](#)]
46. Kim, J.; Dai, S.; Jang, J.; Waite, W.; Collett, T.; Kumar, P. Compressibility and particle crushing of Krishna–Godavari Basin sediments from offshore India: Implications for gas production from deep-water gas hydrate deposits. *Mar. Pet. Geol.* **2018**, *108*, 697–704. [[CrossRef](#)]
47. Kozeny, J. *Ueber Kapillare Leitung des Wassers im Boden*; Sitzungsber Akad. Wiss.: Wiena, Austria, 1927; Volume 13, pp. 271–306.
48. Carman, P. Permeability of saturated sands, soils and clays. *J. Agric. Sci.* **1939**, *29*, 262–273. [[CrossRef](#)]
49. Matyka, M.; Khalili, A.; Koza, Z. Tortuosity-porosity relation in porous media flow. *Phys. Rev. E* **2008**, *78*, 026306. [[CrossRef](#)] [[PubMed](#)]
50. Terzaghi, K. Soil failure at barrages and its prevention. *Spec. Forchh. Issue Die Wasserkr.* **1922**, *17*, 445–449.
51. Ren, X.W.; Santamarina, J.C. The hydraulic conductivity of sediments: A pore size perspective. *Eng. Geol.* **2018**, *233*, 48–54. [[CrossRef](#)]
52. Dai, S.; Seol, Y. Water permeability in hydrate-bearing sediments: A pore-scale study. *Geophys. Res. Lett.* **2014**, *41*, 4176–4184. [[CrossRef](#)]
53. Uchida, S.; Soga, K.; Yamamoto, K. Critical state soil constitutive model for methane hydrate soil. *J. Geophys. Res. Solid Earth* **2012**, *117*, B03209. [[CrossRef](#)]
54. Schofield, A.; Wroth, C. *Critical State Soil Mechanics*; Cambridge Press: Cambridge, UK, 1968.
55. Miyazaki, K.; Tenma, N.; Aoki, K.; Yamaguchi, T. A nonlinear elastic model for triaxial compressive properties of artificial methane-hydrate-bearing sediment samples. *Energies* **2012**, *5*, 4057–4075. [[CrossRef](#)]
56. Sánchez, M.; Santamarina, C.; Teymouri, M.; Gai, X. Coupled numerical modeling of gas hydrate bearing sediments: From laboratory to field-scale analyses. *J. Geophys. Res. Solid Earth* **2018**, *123*, 10326–10348. [[CrossRef](#)]
57. Kim, H.C.; Bishnoi, P.R.; Heidemann, R.A.; Rizvi, S.S.H. Kinetics of methane hydrate decomposition. *Chem. Eng. Sci.* **1987**, *42*, 1645–1653. [[CrossRef](#)]
58. Kamath, V.A.; Holder, G.D. Dissociation heat transfer characteristics of methane hydrates. *AIChE J.* **1987**, *33*, 347–350. [[CrossRef](#)]
59. Yamamoto, K.; Terao, Y.; Fujii, T.; Ikawa, T.; Seki, M.; Matsuzawa, M.; Kanno, T. Operational overview of the first offshore production test of methane hydrates in the Eastern Nankai Trough. In Proceedings of the Offshore Technology Conference, Houston, TX, USA, 5–8 May 2014.